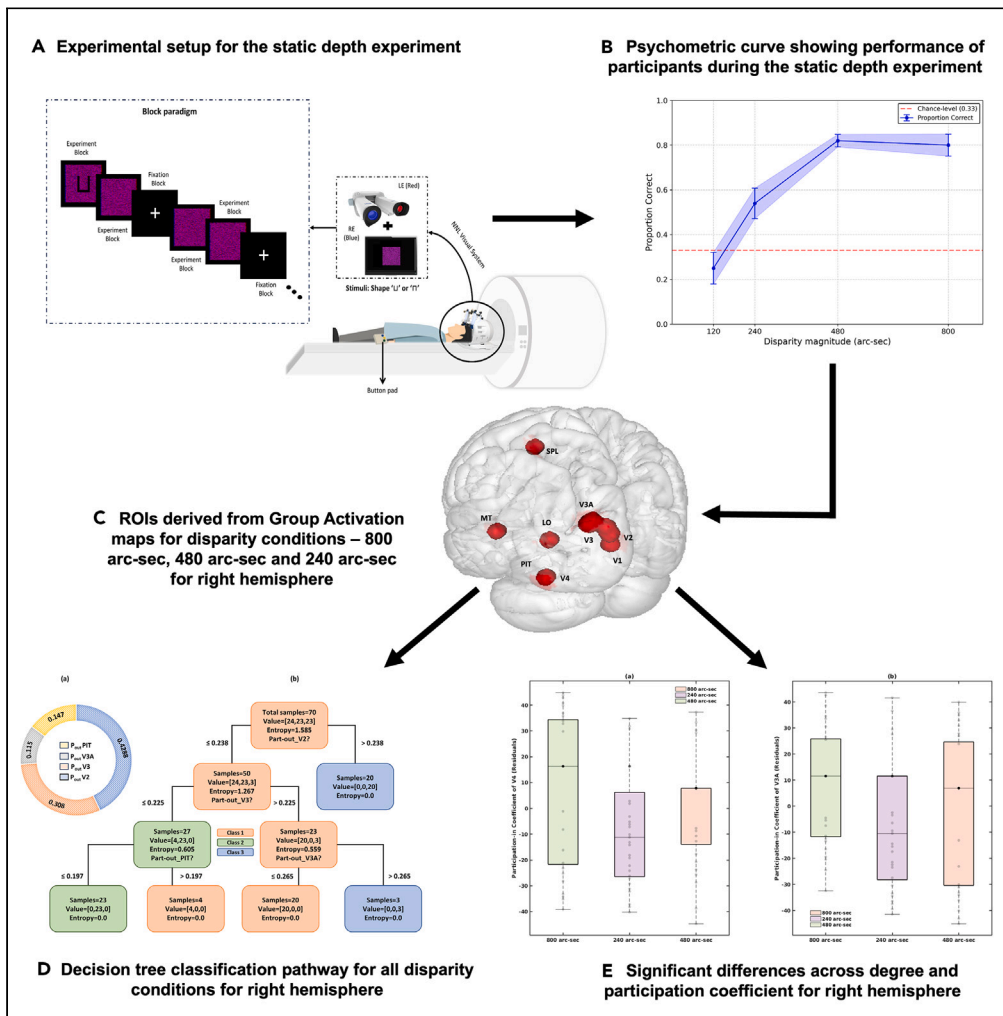


Article

Distinct rich and diverse clubs regulate coarse and fine binocular disparity processing: Evidence from stereoscopic task-based fMRI



Kritika Lohia, Rijul Saurabh Soans, Rohit Saxena, Kabir Mahajan, Tapan K. Gandhi

rijul.soans@berkeley.edu

Highlights

MT is the only common rich and diverse region with a key role in disparity processing

Diverse club members outperform those of rich club in decoding disparity magnitudes

Rich club members contribute to only shape recognition during disparity processing

The right hemisphere of brain is dominant in disparity processing, except for V3A



Article

Distinct rich and diverse clubs regulate coarse and fine binocular disparity processing: Evidence from stereoscopic task-based fMRI

Kritika Lohia,¹ Rijul Saurabh Soans,^{1,2,3,6,*} Rohit Saxena,⁴ Kabir Mahajan,⁵ and Tapan K. Gandhi¹

SUMMARY

While cortical regions involved in processing binocular disparities have been studied extensively, little is known on how the human visual system adapts to changing disparity magnitudes. In this paper, we investigate causal mechanisms of coarse and fine binocular disparity processing using fMRI with a clinically validated, custom anaglyph-based stimulus. We make use of Granger causality and graph measures to reveal the existence of distinct rich and diverse clubs across different disparity magnitudes. We demonstrate that Middle Temporal area (MT) plays a specialized role with overlapping rich and diverse characteristics. Next, we show that subtle interhemispheric differences exist across various brain regions, despite an overall right hemisphere dominance. Finally, we pass the graph measures through the decision tree and found that the diverse clubs outperform rich clubs in decoding disparity magnitudes. Our study sets the stage for conducting further investigations on binocular disparity processing, particularly in the context of neuro-ophthalmic disorders with binocular impairments.

INTRODUCTION

Stereopsis is a fundamental feature of the human visual system (HVS) that is essential for the reconstruction of the depth dimension of the world. The HVS is able to compute this due to the horizontal separation of the eyes that introduce tiny horizontal differences in the retinal images of objects. These differences – termed binocular disparities – are the first step toward the evaluation of stereopsis.¹ Consequently, understanding the underlying neural mechanisms of binocular disparities has important implications, particularly in the assessment and treatment of eye disorders such as strabismus and amblyopia,^{2–11} interaction with virtual reality,^{12,13} and inverse problems in computer vision.^{14–16}

Previous investigations on binocular disparities have revealed the presence of disparity-specific regions across dorsal and ventral visual streams including V3A, MT+/V5, V7, lateral occipital (LO) and intraparietal sulcus (IPS).^{17–22} While these regions serve as the physiological basis for stereoscopic depth perception, the underlying neural activity covaries with disparity magnitudes within detectable ranges²³ across both visual streams. Preston TJ et al.²⁴ found a positive correlation of BOLD signal with the disparity magnitude for dorsal visual stream while having no correlation with the ventral visual stream. Subsequently, Wang F et al.²⁵ utilized a larger range of binocular disparities to investigate this disparity-response curve and confirmed the dominance of the dorsal visual stream; but, they did not find a monotonically increasing functional magnetic resonance imaging (fMRI) response with the disparity magnitude. However, the observed correlation in these studies is not intrinsic but instead arises as a result of specific causal interactions within their integrated network.²⁶ Understanding these causal interactions would provide valuable insights into the neural underpinnings of the variations in stereoacuity thresholds observed among different individuals. For example, higher stereoacuity thresholds have been reported in patients with impaired eye alignment disorders such as amblyopia,⁷ strabismus²⁷ and induced anisometropic populations.²⁸ Moreover, visually healthy controls could also exhibit sub-normal stereoacuity. Deepa et al.²⁹ reported that only around 13% of their tested population met the criterion for the normal level of stereopsis. Almost 45% of their study population had borderline stereopsis and the remaining 42% had reduced stereopsis. If the measuring test is kept the same, then perceptually this can only happen if there is distinct neural processing of varying disparity sizes. Therefore, changes in effective connectivity can serve as important biomarkers for extracting clinically relevant information from patients with impaired stereopsis. Recently, one study³⁰ utilized resting state fMRI to investigate causal interactions among several cortical regions in amblyopic patients. The authors report that the stereoscopic anomalies present in the amblyopic patients may result from the changes in effective connectivity of the higher-order visual regions. However, the use of resting-state functional MRI (rs-fMRI) as an experimental design would limit the interpretations of relationship between the topology

¹Department of Electrical Engineering, Indian Institute of Technology – Delhi, New Delhi, India

²Laboratory of Experimental Ophthalmology, University Medical Center Groningen, University of Groningen, Groningen, the Netherlands

³Herbert Wertheim School of Optometry and Vision Science, University of California, Berkeley, Berkeley, CA, USA

⁴Dr. Rajendra Prasad Centre for Ophthalmic Sciences, All India Institute of Medical Sciences, New Delhi, India

⁵Mahajan Imaging Center, Hauz Khas, New Delhi, India

⁶Lead contact

*Correspondence: rijul.soans@berkeley.edu

<https://doi.org/10.1016/j.isci.2024.109831>



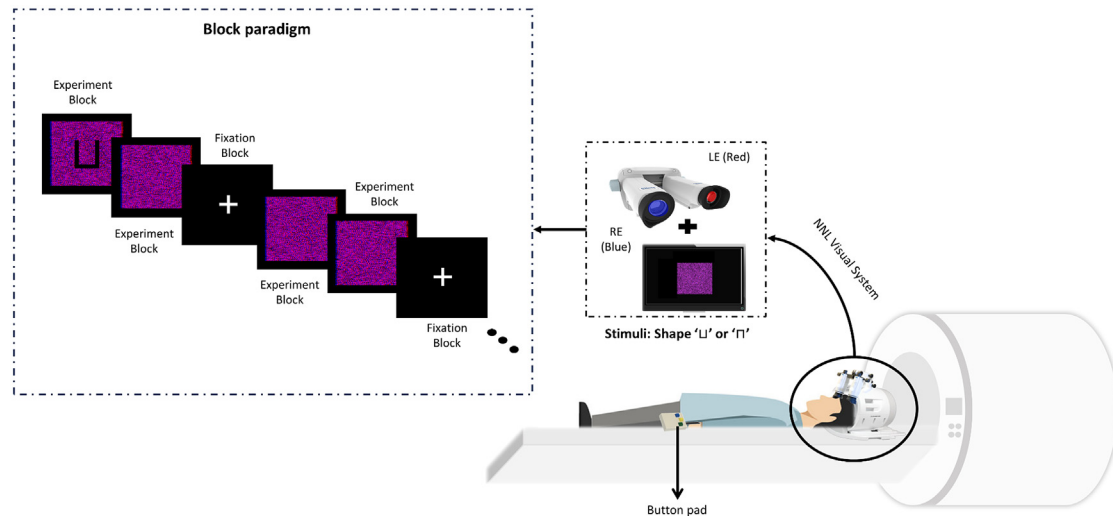


Figure 1. Overall experimental setup at the scanner

Participants lay in supine position in the MR scanner with their left- and right-hand index fingers placed on separate button pads (Lumina 3G controller) to indicate the 3D-shape ('L' or 'Π') in the static depth experiment. The fMRI block design (left inset view) shows the occurrence of two experimental blocks followed by a fixation block wherein each block lasted for 20 s. The 'L' shape in the experimental block is for illustration purposes only. The actual 'L' or 'Π' shape was visible only when viewed stereoscopically with the NNL visual goggles (right inset view) and the superimposed red and blue films on left and right eye, respectively.

of brain networks and the stereoscopic depth perception or to other aspects of brain function.^{31,32} Thus, it remains an open question how the complex topological properties of human brain networks are related to adapting to changing disparity magnitudes. This holds significant importance toward developing a holistic understanding of stereoscopic depth perception.

Our analysis is based on Granger causality (GC)³³ – a widely used approach in exploring brain network causality – functional segregation (within-network connectivity) and functional integration (between-network connectivity).^{34,35} Specifically, we use GC to construct directed networks to derive degree (D) and participation coefficients (PC).³⁶ Each node in the community structure has a distinct role depending upon their D and PC.^{36,37} The high-degree nodes that tend to be closely connected among their communities are called the *rich clubs*,³⁸ whereas the higher PC nodes are called diverse clubs.³⁹ Until recently, the rich club was thought to be critical for global communication and considered as an integrative and stable core of brain regions that coordinates the transmission of information across the network.^{38,40} However, Bertolero MA et al.³⁹ suggested that the higher PC nodes tend to interact even more strongly with other communities. While the brain network changes under different experimental conditions,^{41–43} a comprehensive understanding of rich and diverse clubs can help identify the neural substrate of disparity magnitude processing. Further, in order to investigate the existence of rich-diverse dichotomy under a clinically relevant range of disparity magnitudes, we appropriately modify our digital version (digital stereoacuity test – DST⁴⁴) of a random dot-based test – TNO (The Netherlands Organization) and subsequently utilize it within the fMRI setting. We chose TNO because of its superior performance to contour-based stereotests.^{45,46} Although TNO is one of the most widely used clinical tests for measuring stereopsis, employing well-controlled and clinically comparable stereoscopic stimuli in an fMRI setting can further help aid clinicians in establishing a stronger correlation between TNO thresholds and the fMRI results of the patients.

Another obvious related question concerns the interhemispheric differences associated with disparity processing. Some studies^{23,47,48} have suggested bilateral and right hemispherically inclined roles of areas V3A and IPS, respectively, for the extraction and processing of stereoscopic depth perception. Contrarily, Wang F et al.,²⁵ reported the involvement of V3, V3A and MT + only in the right hemisphere. Moreover, other studies^{19,49} have also identified a general dominance of the right hemisphere in the perceptual processing of stereopsis. These studies provide mixed evidence regarding the processing of disparity across hemispheres. Interestingly, there have been no studies addressing the interhemispheric differences specific to the processing of disparity magnitudes.

In this study, we hypothesized that: (1) there are unique rich and diverse clubs catering to processing of different disparity magnitudes; (2) if the identified rich and/or diverse club members yield a greater disparity-decoding performance and rank higher in feature importance, they are deemed to play significant roles in the processing of disparity magnitudes; (3) there are interhemispheric differences in the significant rich and/or diverse club members across different disparity magnitudes. Overall, our hypotheses revolve around the idea that the rich and diverse clubs play distinct roles in the complex brain topology and further contribute to revealing unique and distinct patterns during stereoscopic depth perception.

RESULTS

Group-level fMRI activations across different disparity magnitudes

Figure 1 illustrates the overall experimental setup and the fMRI block design used in the static depth experiment. The psychometric curve (Figure 2) showed an overall increase in percent correct responses with disparity magnitude except at 480 arc-sec wherein the performance

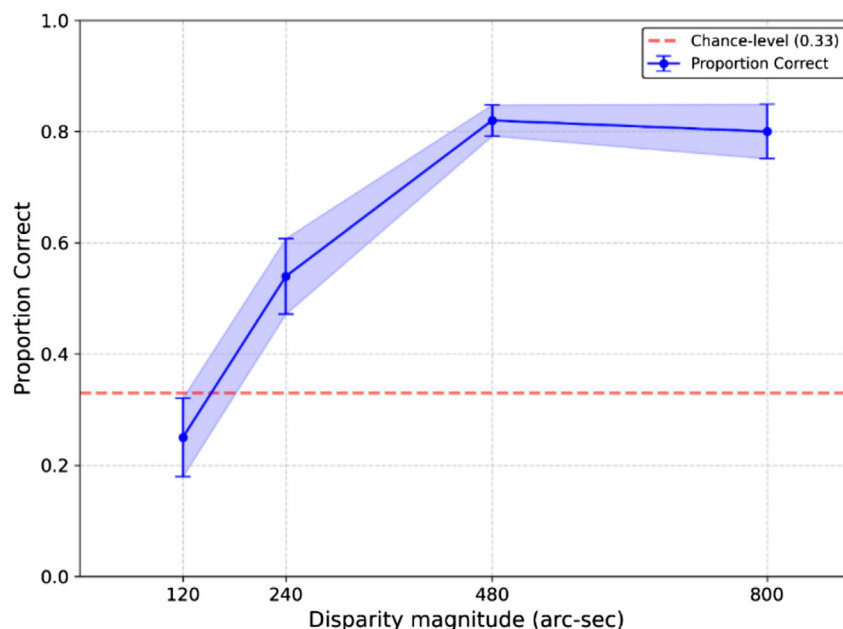


Figure 2. Behavioral performance of the participants for the stereoscopic task

The psychometric curve showing increase in performance of participants ($N = 20$) with the disparity magnitude under the fMRI stereoscopic depth perception task.

was greater compared to 800 arc-sec condition. The 120 arc-sec condition showed a less than chance (P_c : Proportion correct = 0.33) performance and was therefore excluded in further analyses. Next, we performed group analysis followed by cluster correction using *Clustsim* (refer to *STAR methods* section) which revealed activation maps for contrasts 800 > SN (Figure 3A), 480 > SN noise (Figure 3B) and 240 > SN (Figure 3C). The clusters that survived the uncorrected cluster-forming p -threshold of $p < 0.001$ for overall alpha (probability that the given cluster is greater than cluster-size threshold) threshold of $p < 0.05$ for all three conditions are detailed in Table S1. We also observed consistent activations in post-central and pre-frontal cortex pertaining to button-press⁵⁰ and generic task executions^{51,52} in all disparity-task conditions. Since these were not the primary focus of our research hypotheses, we only selected the clusters associated with stereoscopic depth perception task. Further, Table S2 shows the details of all ROIs derived from these clusters across both hemispheres.

Rich and diverse clubs across the right hemisphere

In the next step, we constructed networks by applying GC to the ROIs derived (Table S2) from activation analysis. The D_{avg} and PC_{avg} obtained using BCT across all regions and disparity conditions for RH after removing the effects of shape are shown in Figures S1–S6. Next, we selected the brain regions with high D_{avg} (median-value over 80th percentile and above) and found that the diverse club members included: (1) MT and V4 during 800 arc-sec condition and (2) SPL and MT during 240 arc-sec condition and (3) MT, PIT and V3A during 480 arc-sec condition. By selecting the brain regions with high PC_{avg} (median-value over 80th percentile and above), we found that the rich club members included: (1) V3, MT and SPL during 800 arc-sec, (2) MT and PIT during 240 arc-sec condition, and (3) PIT, V1 and MT during 480 arc-sec condition. The common rich and diverse club members included: (1) MT during the 800 arc-sec condition, (2) MT during the 240 arc-sec condition, and (3) regions MT and PIT during the 480 arc-sec condition. For further analysis, we used the Quade test with shape as a covariate coupled with post-hoc tests (Tukey-Kramer) for pairwise comparisons across 3D conditions that showed: (1) P_{in} coefficient of V4 ($F = 3.71$, $df = 2$; $p = 0.0285$) was significantly different for the 800 and 480 arc-sec conditions (median: 16.344 & -11.155; $p = 0.0211$; see Figure 4A) respectively, (2) P_{in} coefficient of V3A ($F = 3.16$, $df = 2$; $p = 0.0496$) was significantly different for the 800 and 240 arc-sec conditions (median: 11.55 & -10.448; $p = 0.0466$; see Figure 4B) respectively. When shape is not considered as a covariate, following comparisons across 3D conditions are revealed: (1) D_{in} of V4 was significantly different ($F = 3.79$, $df = 2$; $p = 0.0264$) for the 240 and 480 arc-sec conditions (median rank: 46 & 28; $p = 0.0230$) respectively, (2) D_{in} of MT was significantly different ($F = 5.57$, $df = 2$; $p = 0.0054$) for the 240 and 480 arc-sec conditions (median rank: 42.5 & 21; $p = 0.005$) respectively, (3) D_{out} of regions V2 ($F = 3.24$, $df = 2$; $p = 0.0443$) and SPL ($F = 5.76$, $df = 2$; $p = 0.0045$) were significantly different for the 240 and 480 arc-sec conditions (median rank: 59.5 & 33; $p = 0.041$ and median rank: 60.5 & 25.5; $p = 0.011$), (4) P_{in} coefficient of V2 was significantly different ($F = 3.44$, $df = 2$; $p = 0.0365$) for the 800 and 480 arc-sec conditions (median: 57 & 32; $p = 0.0424$) respectively, (5) P_{in} coefficient of V3 was significantly different ($F = 3.37$, $df = 2$; $p = 0.039$) for the 800 and 480 arc-sec conditions (median: 58.5 & 26; $p = 0.046$) respectively, (6) P_{in} coefficient of V4 ($F = 4.95$, $df = 2$; $p = 0.0093$) was significantly different for the 800 and 240 arc-sec conditions (median: 57.5 & 30; $p = 0.0211$) respectively and for 240 and 480 arc-sec conditions (median: 30 & 57.5; $p = 0.017$) respectively, and (7) P_{in} coefficient of V3A was significantly different ($F = 3.27$, $df = 2$; $p = 0.0428$) for the 800 and 240 arc-sec conditions (median: 54 & 32; $p = 0.04$) respectively.

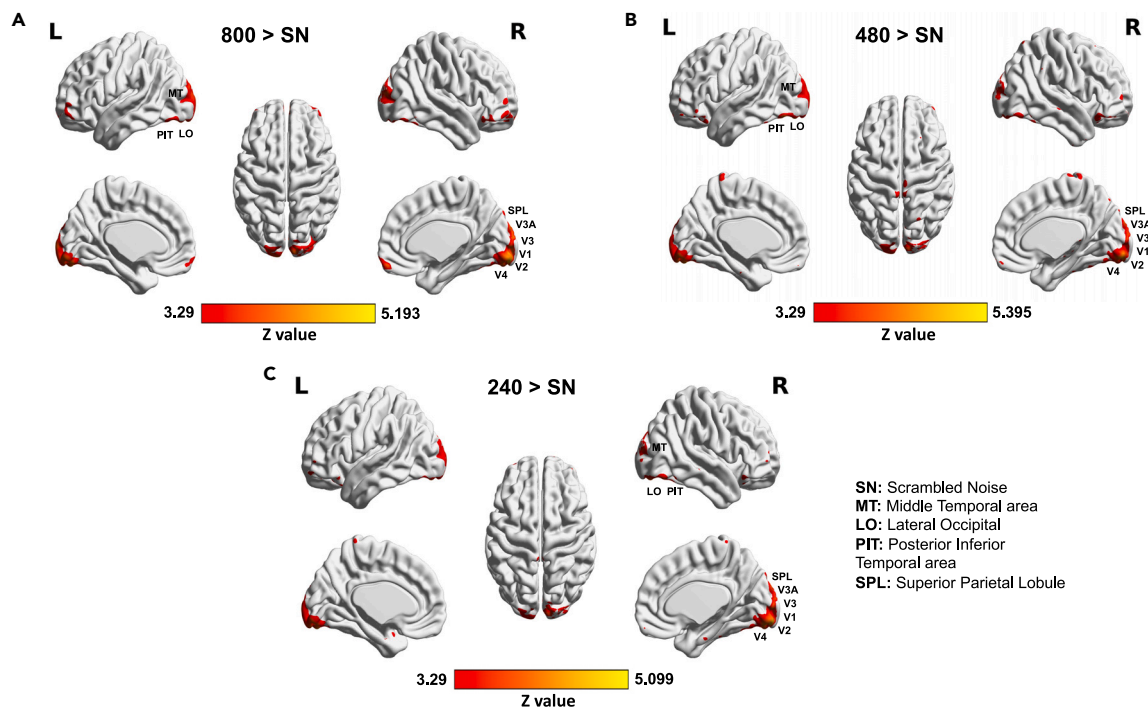


Figure 3. Group fMRI activation patterns for 29 visually healthy participants

(A) Group activations for the GLM contrast [800 > SN] at the cluster defining threshold of $p = 0.001$ (cluster >53 voxels for it to be significant at $p < 0.05$), (B) Group activations for the GLM contrast [480 > SN] at the cluster defining threshold of $p = 0.001$ (cluster >46 voxels for it to be significant at $p < 0.05$), (C) Group activations for the GLM contrast [240 > SN] at the cluster defining threshold of $p = 0.001$ (cluster >45 voxels for it to be significant at $p < 0.05$). The details of activation clusters are mentioned in Tables S1 and S2.

Rich and diverse clubs across the left hemisphere

We follow a similar analysis for LH as we did for RH. The D_{avg} and PC_{avg} are illustrated in Figures S7–S12. The brain regions included in the rich club included: (1) V2, V3A and MT during 800 arc-sec condition, (2) V1, V3A and MT during 240 arc-sec condition and, (3) MT and V3A during 480 arc-sec condition. Meanwhile, the diverse club included: (1) MT and V4 during 800 arc-sec condition, (2) MT and PIT during 240 arc-sec condition, and (3) V1, SPL and MT during 480 arc-sec condition. Further, MT is the only common rich and diverse club region across all disparity conditions. The Quade test with shape as a covariate coupled with post-hoc tests for pairwise comparisons across 3D conditions revealed that the P_{out} coefficient of V1 is significantly different ($F = 3.93$, $df = 2$; $p = 0.0234$) for the 800 and 240 arc-sec condition (median: 17.448 and -18.551 ; $p = 0.017$; see Figure 5) respectively. When shape is not considered as a covariate, following comparisons across 3D conditions are revealed: (1) P_{out} coefficient of V1 is significantly different ($F = 4.92$, $df = 2$; $p = 0.0095$) for the 800 and 240 arc-sec condition (median rank: 64 and 28; $p = 0.017$) respectively and the 800 and 480 arc-sec condition (median rank: 64 and 28; $p = 0.0278$) respectively and (2) P_{out} coefficient of V2 is significantly different ($F = 3.41$, $df = 2$; $p = 0.0376$) for the 800 and 480 arc-sec condition (median: 55 and 33; $p = 0.048$) respectively.

Decoding disparity magnitude with diverse club members across right hemisphere

The input features of DT consisted of both P_{in} and P_{out} coefficients of all ROIs and all disparity conditions (800 arc-sec, 480 arc-sec, and 240 arc-sec) as described in STAR methods section. Figure 6B shows the DT model that was trained to classify disparity conditions based on the above-mentioned features. The model identified the best parameters (criterion: entropy, max depth: 4, min sample: 2 and splitter: best) using a 5-fold grid search cross validation to optimize the hyperparameters and was able to classify with precision: 0.9523, recall: 0.944, and F1 score: 0.944. The weight assigned to each feature (i.e., feature importance) by the decision tree algorithm is mentioned in Figure 6A.

Decoding disparity magnitude with rich club members across right hemisphere

Unlike the P_{in} and P_{out} coefficients across each node, the D_{in} and D_{out} features did not result in accurate classification. The performance of the decision tree model was poor with precision: 0.462, recall: 0.412, and F1 score: 0.40. Consequently, to investigate whether this low performance was due to the higher similarity in the processing of any two disparity magnitudes or the poor decoding of disparity magnitudes by rich clubs, we trained the decision tree classifier pairwise. The model performance, however, above chance level (>33%),

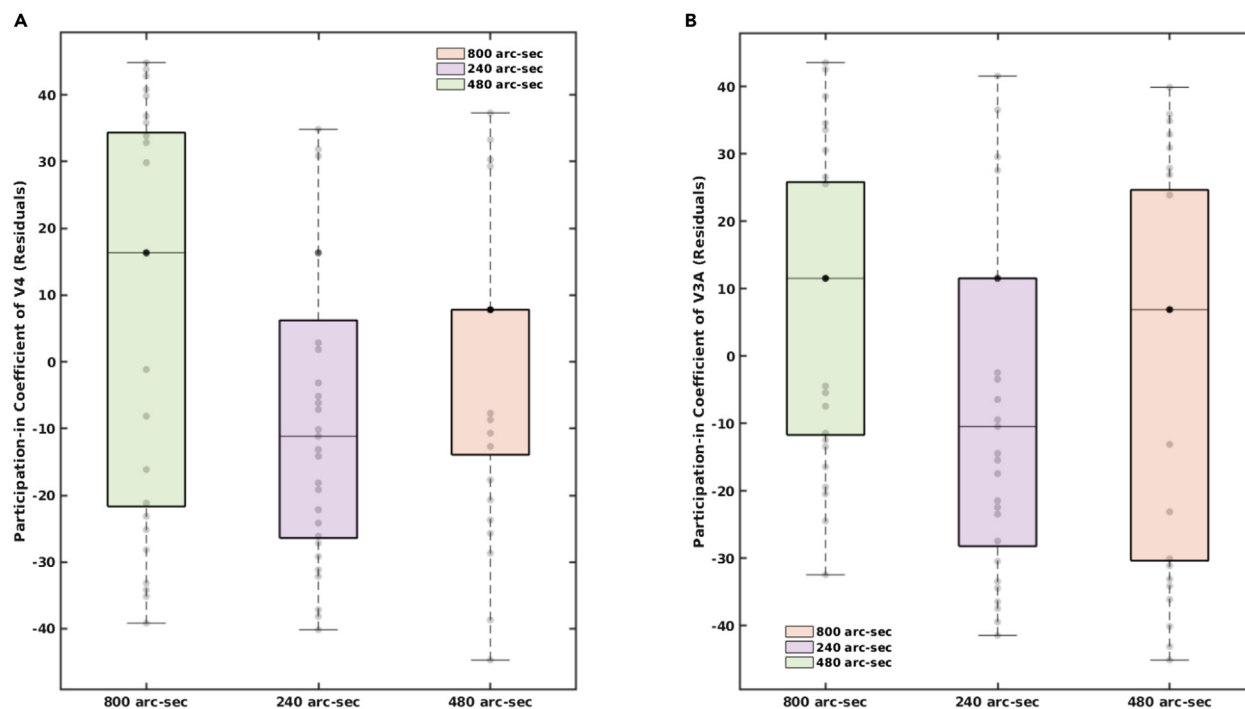


Figure 4. Significant differences in participation coefficients across right hemisphere

(A) Participation-in coefficient of region V4 is significantly different for the 800 and 480 arc-sec conditions (median: 16.344 & -11.155 ; $p = 0.0211$), (B) Participation-in coefficient of V3A is significantly different for the 800 and 240 arc-sec conditions (median: 11.55 & -10.448 ; $p = 0.0466$).

was still worse when compared to diverse clubs in all three pairwise conditions – class 1 vs. class 2 (precision: 0.65, recall: 0.66, and F1 score: 0.649), class 2 vs. class 3 (precision: 0.45, recall: 0.458, and F1 score: 0.386) and class 1 vs. class 3 (precision: 0.65, recall: 0.66, and F1 score: 0.649).

Decoding disparity magnitude with diverse club members across left hemisphere

We followed a similar approach for LH as for RH and trained our model with P_{in} and P_{out} coefficients of all ROIs. The decision tree algorithm (shown in Figure 7B) could decode the disparity conditions with precision: 0.875, recall: 0.834 and F1 score: 0.826. The weight assigned to each feature by the decision tree algorithm is mentioned in Figure 7A.

Decoding disparity magnitude with rich club members across left hemisphere

The decision tree model was trained with D_{in} and D_{out} features for all ROIs. As expected, the model performed similarly to the right hemisphere for the rich clubs with precision: 0.45, recall: 0.28, and F1 score: 0.243.

Differences between right and left hemisphere

Wilcoxon signed Rank test revealed that PC_{avg} was significantly different across several brain regions in LH and RH. The boxplot visualization of each significant finding is shown in Figures S13 to S21 and the corresponding statistical values are mentioned Table 1. There were no other significant inter-hemispheric differences among the remaining conditions.

DISCUSSION

The main findings of our study indicate that the effective connectivity between brain regions changes with the disparity magnitude for visually healthy controls. Specifically, our results reveal the presence of distinct rich and diverse clubs that vary across different disparity magnitudes. Furthermore, our analysis indicates that the MT region serves as the only common rich and diverse region across all disparity magnitudes and in both hemispheres. We also find that diverse clubs exhibit better performance in decoding disparity magnitudes, thereby providing further support to the growing evidence that diverse clubs are indeed the integrative core for processing disparities. Finally, we find that subtle inter-hemispheric differences exist across disparity conditions. Below, we discuss these findings in more detail.

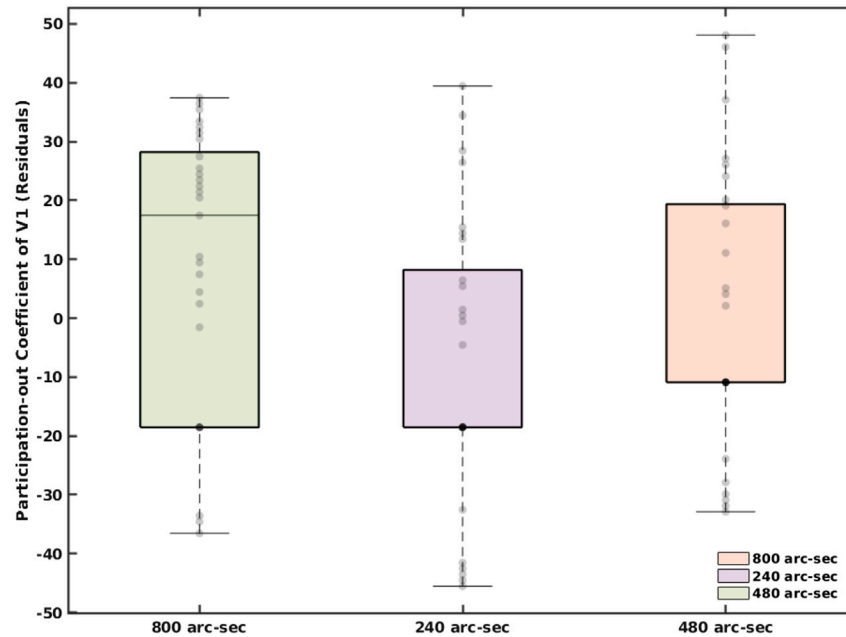


Figure 5. Significant differences in participation coefficients across left hemisphere

Participation-out coefficient of V1 is significantly different for the 800 and 240 arc-sec condition (median: 17.448 and -18.551 ; $p = 0.017$). The black line in the middle of each box represents the median, and the solid black dot represents the mean.

Distinct rich and diverse clubs exist under different disparity magnitudes

The pairwise comparisons of D_{in} , D_{out} and P_{in} , P_{out} (representing rich and diverse club nature, respectively) in the Quade analysis revealed significant differences across several ROIs under different disparity magnitudes. Surprisingly, after removing the effects of disparity shape

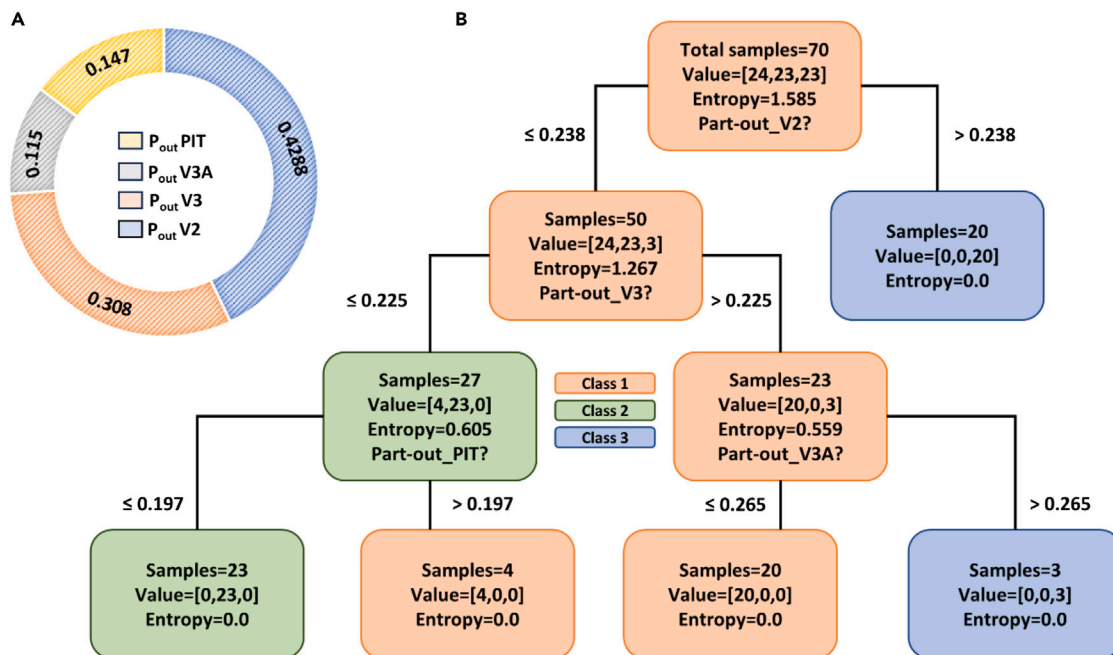


Figure 6. Decoding disparity magnitudes with diverse club members across right hemisphere

(A) Feature importance as evaluated by the Decision tree model for decoding disparity magnitudes, (B) Diverse club decision tree model for classifying disparity conditions – 800 arc-sec (class 1), 240 arc-sec (class 2) and 480 arc-sec (class 3) across right hemisphere. The value set at each level of the tree indicates the number of correctly classified and misclassified disparity conditions.

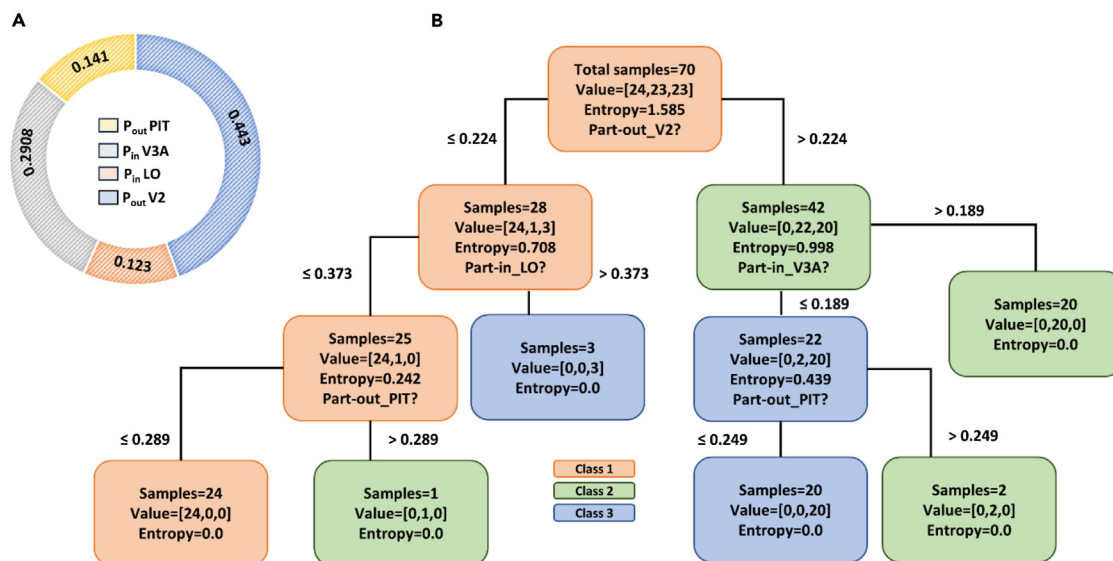


Figure 7. Decoding disparity magnitudes with diverse club members across left hemisphere

(A) Feature importance as evaluated by the Decision tree model for decoding disparity magnitudes, (B) Diverse club decision tree model for classifying disparity conditions – 800 arc-sec (class 1), 240 arc-sec (class 2) and 480 arc-sec (class 3) across left hemisphere. The value set at each level of the tree indicates the number of correctly classified and misclassified disparity conditions.

(‘LJ’ or ‘LΓ’) in the Quade analysis, we found significant differences across different disparity magnitudes solely in the PC, while differences across D were no longer significant. Specifically for RH, participants viewing 800 arc-sec condition exhibited a significantly higher P_{in} for both V4 and V3A as compared to 240 arc-sec condition (Figure 4). The fluctuations in PC observed over the range of disparities are expected as the fMRI response itself does not have a strictly monotonic relationship with disparity magnitude.^{23–25,53} Backus et al.²³ found that mean response in early visual areas is a bimodal function of disparity magnitude, where BOLD activity first increases from 30 to 60 arc-sec, then decreases until 225 arc-sec, and finally rises to 900 arc-sec. However, in our study we found that the differences across early visual areas (P_{in} for V2 and V3) were rather contributing to the 3D-shape characteristic of the disparity conditions. Further, we argue that the existence of significantly different diverse and not rich clubs may explain distinct neural mechanisms beyond the interpretation of BOLD activity changes alone.

In the subsequent subsections, we explain the region-wise contributions in decoding disparity magnitudes obtained from DT analysis. We focus only on the RH due to its higher DT-classification performance compared to LH.

Common stereo processing until V2

Despite having a significantly higher P_{in} in region V2 for 480 arc-sec condition compared to both 240 arc-sec conditions, the DT classification pathway starts with a common region (Figure 6B) V2 for all disparity magnitudes. This may be because early visual areas provide crude yet important representations of disparity^{20,54} to the extent that lesions to them can lead to impaired stereoacuity.^{55–57} Moreover, the shared utilization of V2 across all disparity magnitudes could also be reasoned with the “correspondence problem” in stereopsis. For the visual

Table 1. Interhemispheric differences in the average participant coefficients

SNo.	ROI	Signed Rank & Z	p value	Disparity Magnitude (arc-sec)	Median: RH & LH
1	V2	126 & -1.97	0.047	800	0.26 & 0.19
2	PIT	329 & 2.411	0.0159	800	0.25 & 0.19
3	V3A	338 & 2.6	0.0092	800	0.191 & 0.26
4	V3	324 & 2.3	0.021	240	0.39 & 0.188
5	PIT	328 & 2.38	0.0169	240	0.324 & 0.208
6	V3A	379 & 3.49	4.70E-04	240	0.212 & 0.19
7	V3	326 & 2.34	0.019	480	0.36 & 0.19
8	V3A	86 & -2.84	0.0045	480	0.18 & 0.24
9	SPL	55 & -3.513	4.40E-04	480	0.27 & 0.18

Overall dominance of right hemisphere for all identified brain regions except for region V3A is seen across different disparity magnitudes. The differences are significant at $p < 0.05$.

system to match features in the left eye with the corresponding features in the right eye, it must reject a large number of possible local matches between the images of the two eyes while preserving the correct matches. This entire corresponding feature matching across eyes takes place in the extrastriate cortex,⁵⁸ with specialization for relative disparity processing in V2,⁵⁹ irrespective of the disparity magnitude.

Role of V3A and PIT in decoding disparity magnitudes

In our experiment, V3A discriminated between 800 (coarse) and 480 arc-sec (mid) disparity magnitudes. There could be three reasons for this: 1) V3A neurons are highly sensitive^{18,23,48,60,61} toward discriminating disparity magnitudes in general, 2) V3A specifically aids in encoding mid-level disparities. However, the range of disparity categorized as coarse, mid or relatively fine is subject to its definition by the experimenter. For instance – Chen et al.⁶² used disparities less than 600 arc-sec in their “smallest detectable disparity” experiment and concluded the role of V3A in decoding the finer disparity signals. Although we refer to 480 arc-sec as a mid-range disparity, our finding is in line with Chen et al.,⁶² 3) V3A is exclusively a diverse club member during the 480 arc-sec condition defined by a higher PC (>0.292 for 480 arc-sec when compared with <0.292 for 800 arc-sec) that in turn aided the decoding. Furthermore, PIT effectively distinguishes between 800 (coarse) and 240 arc-sec (relatively finer) disparity magnitudes (Figure 6B). Notably, as these conditions represent the largest and smallest disparities in our analysis, PIT neurons likely exhibit sensitivity in discriminating between both ranges. While limited evidence exists in humans,⁶³ non-human primate studies link PIT to fine^{64,65} and relatively coarse depth discrimination tasks.⁶⁶

The rich and diverse nature of MT

MT exhibited remarkable overlapping rich and diverse properties across disparity magnitudes and both hemispheres. While MT is known to have a selective preference for disparity processing,^{67–70} intriguingly, the decision tree algorithm did not reveal MT as a prominent feature in decoding disparity magnitudes. This finding could be attributed to MT’s consistent contribution across all disparity magnitudes, encompassing coarse, mid, and relatively finer ranges. Notably, Uka, T., & DeAngelis, G. C.⁷¹ and Neri, P et al.⁴⁷ argue MT to be a part of the neural substrate underlying only coarser disparities. Contrarily, Krug, K., & Parker, A. J.⁷² utilized a wide range of disparities (0–4320 arc-sec) and summarized that V5/MT neurons are also selective for relative disparity. However, their distinction of fine and coarse disparities is based on the type of task employed – absolute (coarse) vs. relative (fine) – rather than the magnitude of test disparities itself.

Although our experiment is designed to test disparity magnitudes with only relative disparities, our findings emphasize that the dual – rich and diverse – characteristic of MT imply its possible contribution to the primitive stereo processing required for all disparity magnitudes rather than being exclusively dedicated to coarser or finer disparities.

Diverse clubs than rich clubs are indeed integrative core in stereo processing

We found that diverse clubs outperformed rich clubs in predicting disparity magnitudes. Additionally, significant differences were observed exclusively across PC for both hemispheres. This provides compelling evidence that PC is a better indicator of the underlying neural mechanisms of disparity magnitudes as opposed to D, which merely measures node connections within or between networks. Our findings align with the recent evidence³⁹ which indicates that diverse clubs exhibit characteristics of an integrative network function to a larger extent compared to rich clubs. Besides, the rich clubs primarily serve to facilitate the formation of specialized subnetworks.³⁸ While rich and diverse clubs may play distinct roles in the brain network communication,⁷³ intuitively, this points to a possibility that the rich clubs are more involved in functional segregation than integration. Considering the global nature of functional integration and its association with diverse clubs, this may be a plausible basis for their superior performance over rich clubs in decoding disparity magnitudes.

Inter-hemispheric differences across disparity magnitudes

Table 1 highlights the significant inter-hemispheric differences in the average PC across V2, V3, V3A, PIT, and SPL. Conforming to the previous studies,^{19,49,74} we found an overall larger involvement of RH in the perception of stereopsis across regions V2, V3, PIT and SPL. This is in line with our preliminary findings⁷⁵ with fewer participants ($n = 11$) where we found that SPL facilitates functional integration for the mid-level disparity magnitude. Besides, SPL is known to exhibit a right hemispheric bias^{19,48,76,77} in the disparity processing. Contrary to SPL, the interpretation of hemispheric dominance in V3A is unclear with previous studies suggesting a bilateral^{18,23,47,78} and right hemispheric dominance.²⁵ In our study, we found RH dominance during 240 arc-sec and LH dominance during 800 and 480 arc-sec conditions. This leads to the possible dependence of hemispheric asymmetry of V3A on the magnitude of disparity. Therefore, except for V3A, we suggest an overall dominance of RH in stereo processing at least for the regions analyzed in our study.

The advantage of a stereoscopic task-based effective connective study over resting-state studies

Overall, our study builds upon previous research highlighting aberrant functional connectivity in the primary⁷⁹ and higher-order visual cortex.⁸⁰ The only study that we can compare our results to is that by Chen et al.³⁰ They used Dynamic Causal Modeling from resting state fMRI to highlight connectivity abnormalities (V2 to LO) in amblyopic patients. They report abnormal effective connectivity specifically in V3d, V3A, V3B, and LO regions (they state them as “important nodes” in the network) by comparing the networks for amblyopic patients and visually healthy controls. Our results are consistent in terms of node-wise importance during stereoscopic depth perception. However, it is important to note that their findings stem from topological comparison between the two groups in the absence of a stereoscopic depth perception task. Therefore, their results represent the intrinsic states of amblyopic visual system

and restricts the extent to which their findings can be meaningfully interpreted. On the other hand, our study is specific and designed for a deeper understanding of the neural mechanisms under various disparity magnitudes in a controlled stereoscopic depth perception task. These advantages contribute to a nuanced understanding of neural mechanisms behind stereoscopic depth perception as previously demonstrated by Liu et al.⁶¹ Moreover, the existence of distinct rich and diverse club patterns across different disparity magnitudes may explain the physiological basis for the variability in stereoacuities reported in visually healthy individuals.²⁹ Our results provide complementary functional evidence to the structural evidence demonstrated by Oishi et al.⁸¹ Notably, our findings also shed light on distinct rich and diverse club patterns across disparity magnitudes and may have potential implications for understanding eye misalignment disorders.

Limitations of the study

There are some limitations to our present study. The NNL goggles are limited in terms of their resolution and FOV.⁸² This may have negatively impacted the participants' performance during the 120 arc-sec disparity condition. Therefore, using some of the latest fMRI-compatible binocular devices with improved display capabilities⁸³ to investigate smaller disparities would be helpful. We also used anaglyph-based stereoscopic stimuli in our investigations. While this was by design so that we could validate the stimulus against the clinically used TNO depth test, future studies could make use of natural and ecologically valid 3D stimuli to confirm whether our findings extend to them.

STAR★METHODS

Detailed methods are provided in the online version of this paper and include the following:

- KEY RESOURCES TABLE
- RESOURCE AVAILABILITY
 - Lead contact
 - Materials availability
 - Data and code availability
- EXPERIMENTAL MODEL AND STUDY PARTICIPANT DETAILS
 - Participants
- METHOD DETAILS
 - MRI acquisition
 - Stimuli and procedure
- QUANTIFICATION AND STATISTICAL ANALYSIS
 - fMRI data analysis
 - Network construction with Granger Causality
 - Definition of rich and diverse clubs
 - Decoding disparity magnitudes

SUPPLEMENTAL INFORMATION

Supplemental information can be found online at <https://doi.org/10.1016/j.isci.2024.109831>.

ACKNOWLEDGMENTS

This study received funding from the Department of Science and Technology - Cognitive Science Research Initiative Project #RP03962G, Govt. of India. The funding organizations had no role in the design, conduct or analysis of this research.

AUTHOR CONTRIBUTIONS

Conceptualization, K.L., R.S.S., T.K.G., and R.S.; Methodology, K.L. and R.S.S.; Formal Analysis: K.L.; Investigation, K.L., R.S.S., R.S., K.M., and T.K.G.; Writing – Original Draft, K.L. and R.S.S.; Writing – Review and Editing, K.L., R.S.S., R.S., K.M., and T.K.G.; Funding Acquisition, T.K.G. and R.S.; Resources, R.S., K.M., and T.K.G.; Supervision, R.S. and T.K.G.

DECLARATION OF INTERESTS

The authors declare no competing interests.

Received: November 9, 2023

Revised: March 7, 2024

Accepted: April 24, 2024

Published: April 26, 2024

REFERENCES

- Gonzalez, F., and Perez, R. (1998). Neural mechanisms underlying stereoscopic vision. *Prog. Neurobiol.* 55, 191–224. [https://doi.org/10.1016/S0301-0082\(98\)00012-4](https://doi.org/10.1016/S0301-0082(98)00012-4).
- Birch, E.E., Stager, D.R., and Everett, M.E. (1995). Random Dot Stereoacuity Following Surgical Correction of Infantile Esotropia. *J. Pediatr. Ophthalmol. Strabismus* 32, 231–235. <https://doi.org/10.3928/0191-3913-19950701-07>.
- Birch, E.E., Fawcett, S., and Stager, D.R. (2000). Why does early surgical alignment improve stereoacuity outcomes in infantile esotropia? *J. AAPOS* 4, 10–14. [https://doi.org/10.1016/S1091-8531\(00\)90005-3](https://doi.org/10.1016/S1091-8531(00)90005-3).
- Fawcett, S., Leffler, J., and Birch, E.E. (2000). Factors influencing stereoacuity in accommodative esotropia. *J. Am. Assoc. Pediatr. Ophthalmol. Strabismus* 4, 15–20. [https://doi.org/10.1016/S1091-8531\(00\)90006-5](https://doi.org/10.1016/S1091-8531(00)90006-5).
- Birch, E.E., and Wang, J. (2009). Stereoacuity outcomes after treatment of infantile and accommodative esotropia. *Optom. Vis. Sci.* 86, 647–652. <https://doi.org/10.1097/OPX.0b013e3181a6168d>.
- Mehner, L., Ng, S.M., and Singh, J. (2023). Interventions for infantile esotropia. *Cochrane Database Syst. Rev.* 1. <https://doi.org/10.1002/14651858.CD004917.pub4>.
- Levi, D.M., Knill, D.C., and Bavelier, D. (2012). Stereopsis and amblyopia: A mini-review HHS Public Access. *Vis. Res.* 114, 17–30. <https://doi.org/10.1016/j.visres.2015.01.002>. Stereopsis.
- Webber, A.L., and Wood, J. (2005). Amblyopia: Prevalence, natural history, functional effects and treatment. *Clin. Exp. Optom.* 88, 365–375. <https://doi.org/10.1111/j.1444-0938.2005.tb05102.x>.
- Grant, S., Melmoth, D.R., Morgan, M.J., and Finlay, A.L. (2007). Prehension deficits in amblyopia. *Invest. Ophthalmol. Vis. Sci.* 48, 1139–1148. <https://doi.org/10.1167/iovs.06-0976>.
- Niechwiej-Szwedo, E., Kennedy, S.A., Colpa, L., Chandrakumar, M., Goltz, H.C., and Wong, A.M.F. (2012). Effects of induced monocular blur versus anisometropic amblyopia on saccades, reaching, and eye-hand coordination. *Invest. Ophthalmol. Vis. Sci.* 53, 4354–4362. <https://doi.org/10.1167/iovs.12-9855>.
- Suttle, C.M., Melmoth, D.R., Finlay, A.L., Sloper, J.J., and Grant, S. (2011). Eye-hand coordination skills in children with and without amblyopia. *Invest. Ophthalmol. Vis. Sci.* 52, 1851–1864. <https://doi.org/10.1167/iovs.10-6341>.
- Wainman, B., Pukas, G., Wolak, L., Mohanraj, S., Lamb, J., and Norman, G.R. (2020). The Critical Role of Stereopsis in Virtual and Mixed Reality Learning Environments. *Anat. Sci. Educ.* 13, 401–412. <https://doi.org/10.1002/ase.1928>.
- Levi, D.M. (2023). Applications and implications for extended reality to improve binocular vision and stereopsis. *J. Vis.* 23, 14. <https://doi.org/10.1167/jov.23.1.14>.
- Poggio, T., Torre, V., and Koch, C. (1985). Computational vision and regularization theory. *Nature* 317, 314–319. <https://doi.org/10.1038/317314a0>.
- Pizlo, Z. (2001). Perception viewed as an inverse problem. *Vis. Res.* 41, 3145–3161. [https://doi.org/10.1016/S0042-6989\(01\)00173-0](https://doi.org/10.1016/S0042-6989(01)00173-0).
- Nieder, A. (2003). Stereoscopic vision: Solving the correspondence problem. *Curr. Biol.* 13, 394–396. [https://doi.org/10.1016/S0960-9822\(03\)00319-1](https://doi.org/10.1016/S0960-9822(03)00319-1).
- Balasopoulou, A., Kokkinos, P., Pagoulatos, D., Plotas, P., Makri, O.E., Georgakopoulos, C.D., Vantarakis, A., Li, Y., Liu, J.J., Qi, P., et al. (2017). Symposium Recent advances and challenges in the management of retinoblastoma Globe - saving Treatments. *BMC Ophthalmol.* 17, 1. <https://doi.org/10.4103/jjo.IJO>.
- Goncalves, N.R., Ban, H., Sánchez-Panchuelo, R.M., Francis, S.T., Schluppeck, D., and Welchman, A.E. (2015). 7 Tesla fMRI reveals systematic functional organization for binocular disparity in dorsal visual cortex. *J. Neurosci.* 35, 3056–3072. <https://doi.org/10.1523/JNEUROSCI.3047-14.2015>.
- Nishida, Y., Hayashi, O., Iwami, T., Kimura, M., Kani, K., Ito, R., Shiino, A., and Suzuki, M. (2001). Stereopsis-processing regions in the human parieto-occipital cortex. *Neuroreport* 12, 2259–2263. <https://doi.org/10.1097/00001756-200107200-00043>.
- Roe, A.W., Parker, A.J., Born, R.T., and DeAngelis, G.C. (2007). Disparity channels in early vision. *J. Neurosci.* 27, 11820–11831. <https://doi.org/10.1523/JNEUROSCI.4164-07.2007>.
- Parker, A.J., Smith, J.E.T., and Krug, K. (2016). Neural architectures for stereo vision. *Philos. Trans. R. Soc. Lond. B Biol. Sci.* 371, 20150261. <https://doi.org/10.1098/rstb.2015.0261>.
- Yoshioka, T.W., Doi, T., Abdolrahmani, M., and Fujita, I. (2021). Specialized contributions of mid-tier stages of dorsal and ventral pathways to stereoscopic processing in macaque. *Elife* 10, e58749–e58776. <https://doi.org/10.7554/eLife.58749>.
- Backus, B.T., Fleet, D.J., Parker, A.J., and Heeger, D.J. (2001). Human cortical activity correlates with stereoscopic depth perception. *J. Neurophysiol.* 86, 2054–2068. <https://doi.org/10.1152/jn.2001.86.4.2054>.
- Preston, T.J., Li, S., Kourtzi, Z., and Welchman, A.E. (2008). Multivoxel pattern selectivity for perceptually relevant binocular disparities in the human brain. *J. Neurosci.* 28, 11315–11327. <https://doi.org/10.1523/JNEUROSCI.2728-08.2008>.
- Wang, F., Yang, W., Zhang, L., Gundran, A., Zhu, X., Liu, J., Li, X., Bao, S., and Gao, S. (2016). Brain activation difference evoked by different binocular disparities of stereograms: An fMRI study. *Phys. Med.* 32, 1308–1313. <https://doi.org/10.1016/j.ejmp.2016.07.007>.
- Hutchison, R.M., and Gallivan, J.P. (2018). Functional coupling between frontoparietal and occipitotemporal pathways during action and perception. *Cortex* 98, 8–27. <https://doi.org/10.1016/j.cortex.2016.10.020>.
- Read, J.C.A. (2015). Stereo vision and strabismus. *Eye* 29, 214–224. <https://doi.org/10.1038/eye.2014.279>.
- Singh, P., Bergaal, S.K., Sharma, P., Agarwal, T., Saxena, R., and Phuljhele, S. (2021). Effect of induced anisometropia on stereopsis and surgical tasks in a simulated environment. *Indian J. Ophthalmol.* 69, 568–572. https://doi.org/10.4103/jjo.IJO_1540_20.
- Deepa, B.M.S., Valarmathi, A., and Benita, S. (2019). Assessment of stereo acuity levels using random dot stereo acuity chart in college students. *J. Fam. Med. Prim. Care* 8, 3850–3853. https://doi.org/10.4103/jfmpc.jfmpc_755_19.
- Chen, X., Liao, M., Jiang, P., Sun, H., Liu, L., and Gong, Q. (2022). Abnormal effective connectivity in visual cortices underlies stereopsis defects in amblyopia. *Neuroimage. Clin.* 34, 103005. <https://doi.org/10.1016/j.nicl.2022.103005>.
- Raichle, M.E., and Snyder, A.Z. (2007). A default mode of brain function: A brief history of an evolving idea. *Neuroimage* 37, 1083–1099. <https://doi.org/10.1016/j.neuroimage.2007.02.041>.
- Crossley, N.A., Mechelli, A., Vértes, P.E., Winton-Brown, T.T., Patel, A.X., Ginestet, C.E., McGuire, P., and Bullmore, E.T. (2013). Cognitive relevance of the community structure of the human brain functional coactivation network. *Proc. Natl. Acad. Sci. USA* 110, 11583–11588. <https://doi.org/10.1073/pnas.1220826110>.
- Friston, K., Moran, R., and Seth, A.K. (2013). Analysing connectivity with Granger causality and dynamic causal modelling. *Curr. Opin. Neurobiol.* 23, 172–178. <https://doi.org/10.1016/j.conb.2012.11.010>.
- Cohen, J.R., and D'Esposito, M. (2016). The segregation and integration of distinct brain networks and their relationship to cognition. *J. Neurosci.* 36, 12083–12094. <https://doi.org/10.1523/JNEUROSCI.2965-15.2016>.
- Horwitz, B., Warner, B., Fitzer, J., Tagamets, M.-A., Husain, F.T., and Long, T.W. (2005). Investigating the neural basis for functional and effective connectivity. Application to fMRI. *Philos. Trans. R. Soc. Lond. B Biol. Sci.* 360, 1093–1108. <https://doi.org/10.1098/rstb.2005.1647>.
- Yeo, B.T.T., Krienen, F.M., Sepulcre, J., Sabuncu, M.R., Lashkari, D., Hollinshead, M., Roffman, J.L., Smoller, J.W., Zöllei, L., Polimeni, J.R., et al. (2011). The organization of the human cerebral cortex estimated by intrinsic functional connectivity. *J. Neurophysiol.* 106, 1125–1165. <https://doi.org/10.1152/jn.00338.2011>.
- Power, J.D., Schlaggar, B.L., Lessov-Schlaggar, C.N., and Petersen, S.E. (2013). Evidence for hubs in human functional brain networks. *Neuron* 79, 798–813. <https://doi.org/10.1016/j.neuron.2013.07.035>.
- van den Heuvel, M.P., and Sporns, O. (2011). Rich-club organization of the human connectome. *J. Neurosci.* 31, 15775–15786. <https://doi.org/10.1523/JNEUROSCI.3539-11.2011>.
- Bertolero, M.A., Yeo, B.T.T., and D'Esposito, M. (2017). The diverse club. *Nat. Commun.* 8, 1277–1310. <https://doi.org/10.1038/s41467-017-01189-w>.
- de Reus, M.A., and van den Heuvel, M.P. (2013). Rich club organization and intermodule communication in the cat connectome. *J. Neurosci.* 33, 12929–12939. <https://doi.org/10.1523/jneurosci.1448-13.2013>.
- Fornito, A., Yoon, J., Zalesky, A., Bullmore, E.T., and Carter, C.S. (2011). General and Specific Functional Connectivity Disturbances in First-Episode Schizophrenia During Cognitive Control Performance. *Biol. Psychiatr.* 70, 64–72. <https://doi.org/10.1016/j.biopsych.2011.02.019>.
- Nicol, R.M., Chapman, S.C., Vértes, P.E., Nathan, P.J., Smith, M.L., Shtyrov, Y., and Bullmore, E.T. (2012). Fast reconfiguration of high-frequency brain networks in response to

- surprising changes in auditory input. *J. Neurophysiol.* 107, 1421–1430. <https://doi.org/10.1152/jn.00817.2011>.
43. Kitzbichler, M.G., Henson, R.N.A., Smith, M.L., Nathan, P.J., and Bullmore, E.T. (2011). Cognitive Effort Drives Workspace Configuration of Human Brain Functional Networks. *J. Neurosci.* 31, 8259–8270. <https://doi.org/10.1523/JNEUROSCI.0440-11.2011>.
44. Lohia, K., Soans, R.S., Raj, D., Saxena, R., and Gandhi, T.K. (2023). Digital Stereo Test (DST): Static stereopsis assessment in simulated and real depth-deficit patients. *J. Vis.* 23, 4574. <https://doi.org/10.1167/jov.23.9.4574>.
45. Ohlsson, J., Villarréal, G., Abrahamsson, M., Cavazos, H., Sjöström, A., and Sjöstrand, J. (2001). Screening merits of the lang II, frisby, randot, titmus, and TNO stereo tests. *J. AAPOS* 5, 316–322. <https://doi.org/10.1067/mpa.2001.118669>.
46. Simons, K. (1981). A Comparison of the Frisby, Random-Dot E, TNO, and Randot Circles Stereotests in Screening and Office Use. *Arch. Ophthalmol.* 99, 446–452. <https://doi.org/10.1001/archophth.1981.03930010448011>.
47. Neri, P., Bridge, H., and Heeger, D.J. (2004). Stereoscopic processing of absolute and relative disparity in human visual cortex. *J. Neurophysiol.* 92, 1880–1891. <https://doi.org/10.1152/jn.01042.2003>.
48. Tsao, D.Y., Vanduffel, W., Sasaki, Y., Fize, D., Knutsen, T.A., Mandeville, J.B., Wald, L.L., Dale, A.M., Rosen, B.R., Van Essen, D.C., et al. (2003). Stereopsis activates V3A and caudal intraparietal areas in macaques and humans. *Neuron* 39, 555–568. [https://doi.org/10.1016/S0896-6273\(03\)00459-8](https://doi.org/10.1016/S0896-6273(03)00459-8).
49. Carmon, A., and Bechtoldt, H.P. (1969). Dominance of the right cerebral hemisphere for stereopsis. *Neuropsychologia* 7, 29–39. [https://doi.org/10.1016/0028-3932\(69\)90042-6](https://doi.org/10.1016/0028-3932(69)90042-6).
50. Horenstein, C., Lowe, M.J., Koenig, K.A., and Phillips, M.D. (2009). Comparison of unilateral and bilateral complex finger tapping-related activation in premotor and primary motor cortex. *Hum. Brain Mapp.* 30, 1397–1412. <https://doi.org/10.1002/hbm.20610>.
51. Koshino, H., Minamoto, T., Ikeda, T., Osaka, M., Otsuka, Y., and Osaka, N. (2011). Anterior Medial Prefrontal Cortex Exhibits Activation during Task Preparation but Deactivation during Task Execution. *PLoS One* 6, e22909. <https://doi.org/10.1371/journal.pone.0022909>.
52. Brass, M., and von Cramon, D.Y. (2002). The Role of the Frontal Cortex in Task Preparation. *Cerebr. Cortex* 12, 908–914. <https://doi.org/10.1093/cercor/12.9.908>.
53. Minini, L., Parker, A.J., and Bridge, H. (2010). Neural modulation by binocular disparity greatest in human dorsal visual stream. *J. Neurophysiol.* 104, 169–178. <https://doi.org/10.1152/jn.00790.2009>.
54. Bridge, H., and Parker, A.J. (2007). Topographical representation of binocular depth in the human visual cortex using fMRI. *J. Vis.* 7, 1–14. <https://doi.org/10.1167/7.14.15>.
55. Cowey, A., and Porter, J. (1979). Brain damage and global stereopsis. *Proc. R. Soc. Lond. B Biol. Sci.* 204, 399–407. <https://doi.org/10.1098/rspb.1979.0035>.
56. Cowey, A., and Wilkinson, F. (1991). The role of the corpus callosum and extra striate visual areas in stereoacuity in Macaque monkeys. *Neuropsychologia* 29, 465–479. [https://doi.org/10.1016/0028-3932\(91\)90005-S](https://doi.org/10.1016/0028-3932(91)90005-S).
57. Bridge, H. (2016). Effects of cortical damage on binocular depth perception. *Philos. Trans. R. Soc. Lond. B Biol. Sci.* 371, 20150254. <https://doi.org/10.1098/rstb.2015.0254>.
58. Janssen, P., Vogels, R., Liu, Y., and Orban, G.A. (2003). At least at the level of inferior temporal cortex, the stereo correspondence problem is solved. *Neuron* 37, 693–701. [https://doi.org/10.1016/S0896-6273\(03\)00023-0](https://doi.org/10.1016/S0896-6273(03)00023-0).
59. Thomas, O.M., Cumming, B.G., and Parker, A.J. (2002). A specialization for relative disparity in V2. *Nat. Neurosci.* 5, 472–478. <https://doi.org/10.1038/nn837>.
60. Cottareau, B.R., McKee, S.P., Ales, J.M., and Norcia, A.M. (2011). Disparity-tuned population responses from human visual cortex. *J. Neurosci.* 31, 954–965. <https://doi.org/10.1523/JNEUROSCI.3795-10.2011>.
61. Liu, C., Li, Y., Song, S., and Zhang, J. (2020). Decoding disparity categories in 3-dimensional images from fMRI data using functional connectivity patterns. *Cogn. Neurodyn.* 14, 169–179. <https://doi.org/10.1007/s11571-019-09557-6>.
62. Chen, N., Chen, Z., and Fang, F. (2020). Functional specialization in human dorsal pathway for stereoscopic depth processing. *Exp. Brain Res.* 238, 2581–2588. <https://doi.org/10.1007/s00221-020-05918-4>.
63. Iwami, T., Nishida, Y., Hayashi, O., Kimura, M., Sakai, M., Kani, K., Ito, R., Shiino, A., and Suzuki, M. (2002). Common neural processing regions for dynamic and static stereopsis in human parieto-occipital cortices. *Neurosci. Lett.* 327, 29–32. [https://doi.org/10.1016/S0304-3940\(02\)00353-1](https://doi.org/10.1016/S0304-3940(02)00353-1).
64. Uka, T., Tanabe, S., Watanabe, M., and Fujita, I. (2005). Neural correlates of fine depth discrimination in monkey inferior temporal cortex. *J. Neurosci.* 25, 10796–10802. <https://doi.org/10.1523/JNEUROSCI.1637-05.2005>.
65. Janssen, P., Vogels, R., and Orban, G.A. (2000). Three-dimensional shape coding in inferior temporal cortex. *Neuron* 27, 385–397. [https://doi.org/10.1016/S0896-6273\(00\)00045-3](https://doi.org/10.1016/S0896-6273(00)00045-3).
66. Verhoef, B.E., Bohon, K.S., and Conway, B.R. (2015). Functional architecture for disparity in macaque inferior temporal cortex and its relationship to the architecture for faces, color, scenes, and visual field. *J. Neurosci.* 35, 6952–6968. <https://doi.org/10.1523/JNEUROSCI.5079-14.2015>.
67. Roy, J.P., Komatsu, H., and Wurtz, R.H. (1992). Disparity sensitivity of neurons in monkey extrastriate area MST. *J. Neurosci.* 12, 2478–2492. <https://doi.org/10.1523/jneurosci.12-07-02478.1992>.
68. Maunsell, J.H., and van Essen, D.C. (1983). The connections of the middle temporal visual area (MT) and their relationship to a cortical hierarchy in the macaque monkey. *J. Neurosci.* 3, 2563–2586. <https://doi.org/10.1523/JNEUROSCI.03-12-02563.1983>.
69. DeAngelis, G.C., and Newsome, W.T. (1999). Organization of disparity-selective neurons in macaque area MT. *J. Neurosci.* 19, 1398–1415. <https://doi.org/10.1523/jneurosci.19-04-01398.1999>.
70. Rutschmann, R.M., and Greenlee, M.W. (2004). BOLD response in dorsal areas varies with relative disparity level. *Neuroreport* 15, 615–619. <https://doi.org/10.1097/00001756-200403220-00009>.
71. Uka, T., and DeAngelis, G.C. (2006). Linking neural representation to function in stereoscopic depth perception: Roles of the middle temporal area in coarse versus fine disparity discrimination. *J. Neurosci.* 26, 6791–6802. <https://doi.org/10.1523/JNEUROSCI.5435-05.2006>.
72. Krug, K., and Parker, A.J. (2011). Neurons in dorsal visual area V5/MT signal relative disparity. *J. Neurosci.* 31, 17892–17904. <https://doi.org/10.1523/JNEUROSCI.2658-11.2011>.
73. Xue, C., Sun, H., Hu, G., Qi, W., Yue, Y., Rao, J., Yang, W., Xiao, C., and Chen, J. (2020). Disrupted Patterns of Rich-Club and Diverse-Club Organizations in Subjective Cognitive Decline and Amnesic Mild Cognitive Impairment. *Front. Neurosci.* 14, 575652–575714. <https://doi.org/10.3389/fnins.2020.575652>.
74. Murphy, A.P., Leopold, D.A., Humphreys, G.W., and Welchman, A.E. (2016). Lesions to right posterior parietal cortex impair visual depth perception from disparity but not motion cues. *Philos. Trans. R. Soc. Lond. B Biol. Sci.* 371, 20150263. <https://doi.org/10.1098/rstb.2015.0263>.
75. Lohia, K., Soans, R.S., Saxena, R., and Gandhi, T.K. (2023). Disparity size changes functional integration during stereoscopic viewing: A pilot fMRI study. In 29th Annual Meeting of The Organization for Human Brain Mapping (OHBM). <https://doi.org/10.13140/RG.2.23470.28488>.
76. Kwee, I.L., Fujii, Y., Matsuzawa, H., and Nakada, T. (1999). Perceptual processing of stereopsis in humans: High-field (3.0-tesla) functional MRI study. *Neurology* 53, 1599–1601. <https://doi.org/10.1212/WNL.53.7.1599>.
77. Paggetti, G., Leff, D.R., Orihuela-Espina, F., Mylonas, G., Darzi, A., Yang, G.Z., and Menegaz, G. (2015). The role of the posterior parietal cortex in stereopsis and hand-eye coordination during motor task behaviours. *Cognit. Process.* 16, 177–190. <https://doi.org/10.1007/s10339-014-0641-1>.
78. Poggio, G.F., Gonzalez, F., and Krause, F. (1988). Stereoscopic mechanisms in monkey visual cortex: Binocular correlation and disparity selectivity. *J. Neurosci.* 8, 4531–4550. <https://doi.org/10.1523/jneurosci.08-12-04531.1988>.
79. Mendola, J.D., Lam, J., Rosenstein, M., Lewis, L.B., and Shmuel, A. (2018). Partial correlation analysis reveals abnormal retinotopically organized functional connectivity of visual areas in amblyopia. *Neuroimage. Clin.* 18, 192–201. <https://doi.org/10.1016/j.nicl.2018.01.022>.
80. Dai, P., Zhang, J., Wu, J., Chen, Z., Zou, B., Wu, Y., Wei, X., and Xiao, M. (2019). Altered Spontaneous Brain Activity of Children with Unilateral Amblyopia: A Resting State fMRI Study. *Neural Plast.* 2019, 3681430–3681510. <https://doi.org/10.1155/2019/3681430>.
81. Oishi, H., Takemura, H., Aoki, S.C., Fujita, I., and Amano, K. (2018). Microstructural properties of the vertical occipital fasciculus explain the variability in human stereoacuity. *Proc. Natl. Acad. Sci. USA* 115, 12289–12294. <https://doi.org/10.1073/pnas.1804741115>.
82. Forlim, C.G., Bittner, L., Mostajeran, F., Steinicke, F., Gallinat, J., and Kühn, S. (2019). Stereoscopic Rendering via Goggles Elicits Higher Functional Connectivity During Virtual Reality Gaming. *Front. Hum. Neurosci.* 13, 365. <https://doi.org/10.3389/fnhum.2019.00365>.
83. Jolly, J.K., Sheldon, A.A., Alvarez, I., Gallagher, C., MacLaren, R.E., and Bridge, H.

- (2021). A low-cost telescope for enhanced stimulus visual field coverage in functional MRI. *J. Neurosci. Methods* 350, 109023. <https://doi.org/10.1016/j.jneumeth.2020.109023>.
84. Levi, D.M. (2022). Learning to see in depth. *Vis. Res.* 200, 108082. <https://doi.org/10.1016/j.visres.2022.108082>.
85. Esteban, O., Markiewicz, C.J., Blair, R.W., Moodie, C.A., Isik, A.I., Erramuzpe, A., Kent, J.D., Goncalves, M., DuPre, E., Snyder, M., et al. (2019). fMRIPrep: a robust preprocessing pipeline for functional MRI. *Nat. Methods* 16, 111–116. <https://doi.org/10.1038/s41592-018-0235-4>.
86. Gorgolewski, K., Burns, C.D., Madison, C., Clark, D., Halchenko, Y.O., Waskom, M.L., and Ghosh, S.S. (2011). Nipype: A flexible, lightweight and extensible neuroimaging data processing framework in Python. *Front. Neuroinf.* 5, 13. <https://doi.org/10.3389/fninf.2011.00013>.
87. Dale, A.M., Fischl, B., and Sereno, M.I. (1999). Cortical Surface-Based Analysis. *Neuroimage* 9, 179–194. <https://doi.org/10.1006/nimg.1998.0395>.
88. Friston, K.J., Holmes, A.P., Price, C.J., Büchel, C., and Worsley, K.J. (1999). Multisubject fMRI studies and conjunction analyses. *Neuroimage* 10, 385–396. <https://doi.org/10.1006/nimg.1999.0484>.
89. Glasser, M.F., Coalson, T.S., Robinson, E.C., Hacker, C.D., Harwell, J., Yacoub, E., Ugurbil, K., Andersson, J., Beckmann, C.F., Jenkinson, M., et al. (2016). A multi-modal parcellation of human cerebral cortex. *Nature* 536, 171–178. <https://doi.org/10.1038/nature18933>.
90. Betzel, R.F., and Bassett, D.S. (2017). Multi-scale brain networks. *Neuroimage* 160, 73–83. <https://doi.org/10.1016/j.neuroimage.2016.11.006>.
91. Chen, G., Glen, D.R., Saad, Z.S., Paul Hamilton, J., Thomason, M.E., Gotlib, I.H., and Cox, R.W. (2011). Vector autoregression, structural equation modeling, and their synthesis in neuroimaging data analysis. *Comput. Biol. Med.* 41, 1142–1155. <https://doi.org/10.1016/j.compbiomed.2011.09.004>.
92. Perry, P.O., and Wolfe, P.J. (2012). Null models for network data. <https://doi.org/10.48550/arXiv.1201.5871>.
93. Rubinov, M., and Sporns, O. (2010). Complex network measures of brain connectivity: Uses and interpretations. *Neuroimage* 52, 1059–1069. <https://doi.org/10.1016/j.neuroimage.2009.10.003>.
94. Breiman, L., Friedman, J.H., Olshen, R.A., and Stone, C.J. (2017). *Classification and Regression Trees* (Routledge). <https://doi.org/10.1201/9781315139470>.
95. Guimera, R., and Nunes Amaral, L.A. (2005). Functional cartography of complex metabolic networks. *Nature* 433, 895–900.
96. Guimerà, R., Sales-Pardo, M., and Amaral, L.A.N. (2007). Classes of complex networks defined by role-to-role connectivity profiles. *Nat. Phys.* 3, 63–69. <https://doi.org/10.1038/nphys489>.

STAR★METHODS

KEY RESOURCES TABLE

REAGENT or RESOURCE	SOURCE	IDENTIFIER
Deposited data		
Raw fMRI data	This paper; Open Science Framework	OSF: https://doi.org/10.17605/OSF.IO/RSPV6
Code for Decoding analyses using Decision Tree	This paper; Open Science Framework	OSF: https://doi.org/10.17605/OSF.IO/RSPV6
Software and algorithms		
MATLAB R2020b	Mathworks, Natick, MA	https://www.mathworks.com/
Psychtoolbox-3	Psychtoolbox	Article: https://doi.org/10.1163/156856897X00357
fMRIPrep-21.0.1	NiPreps Community	https://fmriprep.org/en/stable/
AFNI	National Institute of Mental Health	https://afni.nimh.nih.gov/
BCT	Brain Connectivity Toolbox	https://sites.google.com/site/bctnet/
Python	Python Software Foundation	https://www.python.org/

RESOURCE AVAILABILITY

Lead contact

Further information and requests for resources should be directed to and will be fulfilled by the lead contact, Rijul Saurabh Soans (rijul.soans@berkeley.edu).

Materials availability

This study did not generate new unique reagents.

Data and code availability

- Raw data has been deposited at Open Science Framework and is publicly available as of the date of publication. DOIs are listed in the [key resources table](#).
- All original code has been deposited at Open Science Framework and is publicly available as of the date of publication. DOIs are listed in the [key resources table](#).
- Any additional information required to reanalyze the data reported in this paper is available from the [lead contact](#) upon request.

EXPERIMENTAL MODEL AND STUDY PARTICIPANT DETAILS

Participants

Thirty-five visually healthy controls (34 males; mean age: 26.8 ± 3.44 ; Indians) with BCVA of 6/9 (0.67 or ≤ 0.17 logMAR) or better in both eyes participated in the Functional Magnetic Resonance Imaging (fMRI) based static-depth experiment. The data from 6 participants were discarded due to excessive head movement and/or inability to follow instructions during the experiment. Thus, all analyses were based on the data of remaining 29 participants (mean age: 26.34 ± 3.47). All participants were chosen with normal stereoacuity (60 arc-sec) measured with the TNO stereo test. The detailed demographic details of the participants finally included in the study are available in [Table S3](#). All participants were required to answer a post-experiment questionnaire ([supplementary material Appendix: 1](#)) designed to understand qualitative aspects of their performance during the experiment. Participants were well informed of all experiments performed in this study and gave written consent prior to their participation. Participant recruitment and conduct of experiments were approved by ethics committee of All India Institute of Medical Sciences, New Delhi, India (IEC-511/17.06.22). This study was in accordance with the tenets of the Declaration of Helsinki.

METHOD DETAILS

MRI acquisition

Functional MRI data were acquired using a 3.0 T GE Scanner (Discovery MR 750w) equipped with a 32-channel phased-array head coil. The scanning parameters were as follows: TR = 2000 ms, TE = 29 ms, 176 slices, voxel resolution = 3 mm × 3 mm × 3.5 mm, slice thickness = 3 mm, Spacing: 0.5, FOV = 192 mm × 192 mm, flip angle = 65°, 610 volumes. The duration of the BOLD scan was 20 min. Subsequently, a

T1-weighted anatomical image (TR = 15 ms, TE = 6.68 ms, voxel resolution = 0.5 mm × 0.5 mm × 1 mm, FOV = 176 × 176 mm, Flip angle = 10°) was acquired for 5 min. Foam pads were used to reduce scanning noise and minimize head motion.

Stimuli and procedure

We adapted the stimuli from our previously clinically validated stimuli⁴⁴ to align with the display specifications in the fMRI setting. The experiment consisted of a random dot stereogram (RDS) stimulus which was designed using Psychtoolbox v.3.0.17 and MATLAB R2020b. The stereoscopic stimuli differed from our previous DST design in two aspects: (i) The RDS square contained a hidden 3D shape ('L' or 'Π' of disparities 120, 240, 480 & 800 arc-secs) where the 'L' shape appeared during 800 and 240 arc-sec conditions and 'Π' appeared during 480 and 120 arc-sec conditions and, (ii) the size of dots and RDS square were appropriately scaled to fit in the Nordic Neuro Lab (NNL; NordicNeuroLab, Bergen, Norway) Visual System goggles (Resolution: 800 × 600, Refresh rate: 85 Hz, FOV: 28.6° horizontal × 20.3° vertical) used inside the MRI scanner. Red and blue anaglyph filters were superimposed over the left and right eye lenses, respectively. The luminance of the dots as seen through the red lens was 4.6 and 4.3 cd/m² as seen through the blue lens. The stimuli were presented in a blocked-design including 3D-shape ('L' or 'Π'), 2D scrambled-noise (SN) (RDS square without hidden 3D shape) and fixation (+) blocks. Each block was repeated five times except the fixation block, which repeated after every 2 experimental (3D-shape and 2D SN) blocks. Each block lasted 20 s with a total experiment duration of 20 min (excluding 5 min of T1-structural scan). Participants had to indicate the shape hidden in the RDS square with a button press (Lumina 3G controller) inside the scanner (left for 'L' and right for 'Π'). Each participant was subjected to a 1-h task-training session with NNL goggles prior to the start of the actual experiment. This was done to improve the perceptual learning of stereopsis⁸⁴ and keep a fair comparison among the participants.

QUANTIFICATION AND STATISTICAL ANALYSIS

fMRI data analysis

Functional MRI data were minimally preprocessed using fMRIPrep-21.0.1⁸⁵ based on Nipype 1.5.127⁸⁶ and the structural T1 data were preprocessed using FreeSurfer (version: 6.0.0).⁸⁷ The Analysis of Functional Neuroimages (AFNI) programs *3dmerge* (with full width half maximum of 4 mm), *3dcalc* and *3dtrend* were used to spatially smooth, scale and detrend fMRI data, respectively. Next, *3dDeconvolve* was used to perform first-level general linear model analysis to extract voxel-wise response amplitude for 3D disparity conditions, 2D SN and fixation blocks. To control the false positive rate (FPR), AFNI program *3dttest++* was used with the *Clustsim* option for randomization and permutation simulations to produce cluster-level threshold values. Clusters were defined as groups of voxels above the uncorrected significance threshold whose faces or edges touched as the default setting of AFNI. This revealed the minimum size of a voxel cluster needed for a corrected *p* of 0.001. Subsequently, conjunction analysis⁸⁸ was performed to obtain the significant activation clusters across all disparity magnitudes. A region of interest (ROI) of size 5 mm was created at the peak of activation cluster using AFNI programs *3dUndump* and *3dfractionize* across each hemisphere. The ROIs were defined based on the Glasser HCP 2016 surface-based parcellation atlas.⁸⁹ Further, the time series extracted from each ROI was used in the network construction (described in the next section).

Network construction with Granger Causality

The network features can generally be extracted at different topological scales viz. whole brain, across a set of related brain regions, or within a specific ROI.⁹⁰ Here, we find out the causal interactions across the set of regions that were activated during our stereoscopic depth perception task. For this, we extracted the times from each ROI and applied Granger Causality (GC) for each disparity condition. The GC was employed using multivariate auto-regressive modeling (MAR)⁹¹ and the lag selection was based on Akaike Information Criteria (AIC). The subject motion parameters were considered as confounders in the model. Consequently, the MAR modeling resulted in disparity specific weighted path matrices wherein all connections were statistically significant at *p* < 0.05. The code (*1dGC.R*) used to construct these weighted path matrices is publicly available in the AFNI package.

Definition of rich and diverse clubs

The weighted path matrices were randomized with positively and negatively signed connections while preserving the positively and negatively signed in-degree (D_{in}) and out-degree (D_{out}) distributions.⁹² We computed node-wise D_{in} , D_{out} participation-in (P_{in}) and participation-out (P_{out}) coefficients to observe inter-regional differences across disparity magnitudes using the Brain Connectivity Toolbox (BCT)⁹³ wherein, in- and out refer to the incoming and outgoing connections, respectively. To remove any potential effects of 3D-shape ('L' or 'Π'), we performed covariate adjustment by regressing out the shape prior to defining rich and diverse club members across disparity conditions. For this, we ranked all node-wise metrics (D_{in} , D_{out} , P_{in} and P_{out}) and the covariate variable (shape) using tied ranks. Subsequently, we ran a linear regression of the ranks of node-wise metrics on the rank of shape. This process yielded raw residuals for all node-wise metrics. Next, we computed the average degree and participation coefficients from these raw residuals. After that, we defined the brain regions with high (median-value over 80th percentile and above) average degree (D_{avg} , wherein average is over in- and out connections) as the *rich club* members across each disparity condition. This follows the notion that nodes with higher degrees are inclined to connect with each other intensely.³⁸ Subsequently, the brain regions with the high (median-value over 80th percentile and above) average participation coefficient (PC_{avg} , wherein average is over in- and out connections) were defined as *diverse club* members. We opted for a threshold cutoff of the 80th percentile as this is where the normalized club coefficient begins to rise, indicating increased clubness.³⁹ Further, we defined a region

as an *overlapping region* if it was present in both rich and diverse categories and was considered to have the highest importance across all regions because of its higher D and PC.⁷³ We took the same ROIs across each hemisphere in the GC analysis for a matched comparison. Thereafter, we performed the Quade test (at $p < 0.05$) by treating 3D shape as a covariate to highlight significant global and local features of these rich and diverse regions across each hemisphere. We also carried post hoc multiple comparisons Tukey Kramer test to determine the group specific differences. Furthermore, we examined the comparisons across disparity conditions without considering 3D-shape as a covariate. This approach allowed us to examine only disparity specific differences by regressing out potential shape differences. This test was used as an alternative to its parametric equivalent – one-way analysis of covariance (ANCOVA).

Decoding disparity magnitudes

The previous analysis yielded rich and diverse club members across different disparity magnitudes. Next, in order to examine the ability of rich and diverse clubs in decoding different disparity magnitudes, we trained a decision tree (DT) model⁹⁴ based on the 3 disparity conditions (800 arc-sec, 240 arc-sec and 480 arc-sec). However, the rich or diverse nature of a region depends on the magnitude of disparity and therefore a region may not always be considered under the rich or diverse categories. While previous studies^{95,96} have generically described participation coefficient as a metric for the diverse nature of a node, we utilized the P_{in} and P_{out} coefficients of all ROIs for the decoding analysis with diverse clubs. Similarly, we use D_{in} and D_{out} for the decoding analysis with rich clubs. Furthermore, DT models are white-box models known for their easy interpretability and their ability to provide feature importance scores. The input features were organized into a matrix with dimensions $[D, M]$, wherein: D represented the product of the number of participants and the number of disparity conditions ($D = 87$), M represented the total number of features ($M = 18$), comprising both P_{in} and P_{out} coefficients of all ROIs. The output was a categorical variable of size $[D, 1]$. These input features were then partitioned into training and test sets using stratified k-fold ($k = 5$) cross validation approach wherein the training dataset contained 70 samples in each fold. We also optimized the hyperparameters (impurity criterion, maximum depth of tree, minimum samples in the split and the type of splitter) using a 5-fold grid search cross-validation. We performed this analysis for RH and LH separately to elucidate the interhemispheric differences in decoding disparity magnitude.